Proceedings of ASME Turbo Expo 2019: Turbomachinery Technical Conference and Exposition
GT2019
June 17-21, 2019, Phoenix, Arizona, USA

GT2019-92062

Thermal Development of an Impinging Jet Using Planar Laser Induced Fluorescence (PLIF)

Lesley M. Wright[1] and Sara Seitz[2]

[1]Texas A&M University
Department of Mechanical Engineering
College Station, Texas 77843-3123
Lesley_Wright@TAMU.edu

[2]Baylor University
Department of Mechanical Engineering
Waco, Texas 76798-7356

ABSTRACT

Planar Laser Induced Fluorescence (PLIF) has been demonstrated to investigate a round jet impinging on a flat surface. Detailed thermal field distributions have been obtained near the flat target surface to characterize the wall jet development ensuing from the stagnation point. While PLIF has been demonstrated for combustion applications to measure concentration gradients within a mixture, its application for temperature field measurements is less established. Therefore, the technique was applied to a simple, cylindrical impinging jet. The jet Reynolds number varied with Re_{jet} = 5,000 – 15,000 while the jet – to – target surface spacing varied from H / D = 4 – 10. The cooling jet (T_{jet} ~ 300 K) impinged on a flat, heated surface. The PLIF technique was able to capture the free jet structure and jet development along the target surface. With a short impingement length (H / D = 4), the potential core of the jet strikes the target surface. The thermal gradients captured during the experiments demonstrate the fully turbulent nature of the impinging jet with H / D = 10. The thermal boundary development along the target surface is clearly captured using this fluorescence method. The near wall temperature gradients acquired with the PLIF method have been used to calculate heat transfer coefficients on the heated surface, and these values compare favorably to those measured using a well-established steady state, heat transfer method. The PLIF technique has been demonstrated for this fundamental impingement setup, and it has proven to be applicable to more complex heat transfer and cooling applications.

NOMENCLATURE

A	Convective heat transfer surface area
D	Nozzle (jet) diameter
h	Convective heat transfer coefficient
H	Jet – to – target surface spacing
I	Intensity
$I_{Back\text{-}Blue}$	Temperature independent fluorescence intensity of background images
$I_{Back\text{-}Red}$	Temperature dependent fluorescence intensity of background images
I_{Blue}	Temperature independent fluorescence intensity of toluene / air images
I_N	Normalized fluorescence intensity of toluene / air images
I_{Red}	Temperature dependent fluorescence intensity of toluene / air images
I_{Ref}	Intensity ratio at reference temperature
k_f	Thermal conductivity of cooling air
L	Jet length (jet plate thickness)
Nu	Nusselt number
Nu_{PLIF}	Nusselt number obtained with PLIF method
$Nu_{Traditional}$	Nusselt number obtained from traditional, steady state heat transfer method
R	Radial coordinate (from jet center)
Re_{jet}	Jet Reynolds number ($\rho VD/\mu$)
T	Temperature
T_{jet}	Jet temperature (outlet of nozzle)
T_{Ref}	Reference (room) temperature
T_∞	Ambient temperature
T_{wall}	Wall temperature (from thermocouple)
V	Jet velocity
Z	Axial coordinate (along jet centerline)
η	Non-dimensional temperature
μ	Dynamic viscosity
ρ	Density

INTRODUCTION

Energy demands around the world continue to increase. Not only are the economies of traditionally developed countries continuing to grow, but demands are constantly increasing as less-developed regions around the world are becoming more industrialized. While many forms of power generation exist to meet these demands, gas turbines continue to meet critical needs around the world. Not only do the engines have a desirable power – to – weight ratio for transportation, they can also be brought on-line in a relatively short amount time. With the

availability of natural gas, the wide range of sizes available, and the ability to integrate these engines with other prime movers, the demand for gas turbine engines remains strong.

With more gas turbine engines being put into service each year, it is necessary to improve the efficiency of the engines to generate increased power while lowering operating costs. Increasing the pressure and temperature ratios of the engine will improve the performance of the engines. However, running the engines at elevated temperatures and pressures must be done cautiously to maintain the life of the engine. To combat these extreme conditions, the hot section components of the engine must be cooled.

Efficient cooling schemes are required to reduce the amount of coolant. Modern cooling technology for the engines involves a combination of external and internal cooling. Han et al. [1] provides a comprehensive review of gas turbine cooling technology. Internal cooling requires enhanced heat transfer within the turbine components. Increasing the near wall mixing will lead to enhanced heat transfer from the interior surface of the airfoils. Cooling techniques include jet impingement and turbulence promotors (ribs, dimples, pins, etc.). Jet impingement is used sparingly within the airfoils; although impingement is the most aggressive form of cooling, it also incurs a significant pressure penalty compared to other cooling methods. Typically, an array or matrix of jets are utilized to impinge on a surface. However, this investigation considers the thermal development of a single jet impinging on a hot surface, and additional details are discussed regarding fundamental jet impingement.

With jet impingement, a coolant air stream is forced out of a hole or slot and impinges on a hot surface known as a target surface. An impinging jet consists of three regions: free jet, stagnation, and wall jet. In the free jet region, the flow is unaffected by the target surface. The momentum exchanged between the jet and its surroundings creates an area known as the potential core, where the velocity profile is preserved uniformly. The potential core begins to shrink after the jet exit, due to the development of a shear layer around the jet and the loss of momentum to the surroundings. The potential core entirely disappears about six to seven jet diameters from the orifice exit, and the jet then becomes fully developed [2]. In the stagnation region, as the jet nears the target surface, the structure of the jet changes due to the influence of the surface. The flow velocity decreases in the normal direction because of presence of the wall. Very thin boundary layers develop on the surface that improve heat transfer through the stagnation region.

The heat transfer rate varies based on the nozzle shape, jet Reynolds number, and jet – to – target surface spacing. In the wall jet region, the horizontal accelerating flow converts to a decelerating flow due to the momentum exchange between the flow and surroundings. With increasing distance from the center, as the boundary layer grows thicker along the wall, generally the heat transfer decreases away from the stagnation point. The Nusselt number has its highest value at the center of the jet and its value decreases outward from the stagnation point.

Jet flows are complex to study because they can be impacted by a variety of factors such as nozzle geometry, flow velocity (Reynolds number), and jet – to – target plate spacing. Ashforth-Frost and Jambunathan [3] studied the impact of nozzle geometry and confinement on the potential core length of turbulent jets. It was observed that potential core length was longer for jets with a fully developed jet exit profile.

Comprehensive studies [4 – 6] have been performed on an impinging jet to investigate the impact of different test parameters on the heat transfer distribution. Goldstein et al. [7] presented the impact of jet – to – target plate spacing (H / D) on stagnation point heat transfer. It was shown that for jet – to – target plate spacing smaller than the length of the potential core, the stagnation Nusselt number is relatively low. As the spacing increases, the Nusselt number also increases and reaches it maximum at H / D = 8. This heat transfer improvement is due to diffusion of the turbulence from the shear layer at the edge to the centerline of the jet. Lee et al. [8] offered a similar investigation on the stagnation point heat transfer; the maximum Nusselt number was observed for H / D = 6. The only difference between the two studies corresponded to the potential core length. In a separate study, Ashforth-Frost and Jambunathan [3] stated that the length of potential core impacts the heat transfer rate; it was shown that the Nusselt number reaches its maximum value at a jet – to – target surface spacing approximately 110% of the potential core length. At this location, the turbulence intensity overcomes the velocity loss, and leads to an increase in heat transfer.

The jet – to – target surface spacing also influences the radial heat transfer distribution. Several studies have been performed on single impinging jets with a relativity large jet – to – target plate spacing ($4 < H / D < 58$) [9, 10]. In a study by Mohanty and Tawfek [11], the heat transfer peak is observed at the stagnation point and it declines exponentially as radial distance increases for $R / D < 0.5$. Baughn and Shimizu [12], Huang and El-Genk [13], and Goldstein et al. [7] reported a secondary peak for the heat transfer coefficient. As the jet travels further from the stagnation point, the heat transfer rate reduces due to an increase in the laminar boundary layer thickness. As jets enter the fully turbulent wall region, the heat transfer rate increases, and therefore, a secondary peak is observed [14, 15].

The Nusselt number distribution of a relatively small jet – to – target surface spacing (H / D = 2) is compared to a large one (H / D = 6) by Goldstein and Timmers [16] using constant heat flux at the target surface. It was shown that for the same Reynolds number, the Nusselt number is higher for larger spacing. The flow within the potential core experiences lower turbulence; as the spacing increases, the shear layer mixing diffuses into the jet, and thus the heat transfer is enhanced.

Goldstein et al. [7] studied the jet – to – target surface spacing and Reynolds number in the range of 2 to 10 and 60,000 to 124,000, respectively. In general, it was shown that the heat transfer coefficient is higher at the stagnation point. However, a secondary peak was found based on the jet – to – target surface spacing and Reynolds number. It was seen that a secondary peak occurs at two diameters from the stagnation point. It was shown that the jet – to – target surface spacing of eight has the highest heat transfer coefficient.

Empirical correlations were developed by Goldstein et al. [7] to estimate the heat transfer coefficient for single impinging jets. The correlations express the Nusselt number as a function of Reynolds number and jet – to – target surface spacing for two types of boundary conditions at the target surface: constant temperature and constant heat flux. Equation 1 shows the correlation for the constant surface heat flux condition. As shown, the correlation develops a linear relationship between the Nusselt number and jet – to – target surface spacing. Also, the Nusselt number increases with an increase in jet Reynolds number. According to the correlation, Goldstein et al. stated that a jet – to – target surface spacing of 7.75 provides the maximum average heat transfer coefficient.

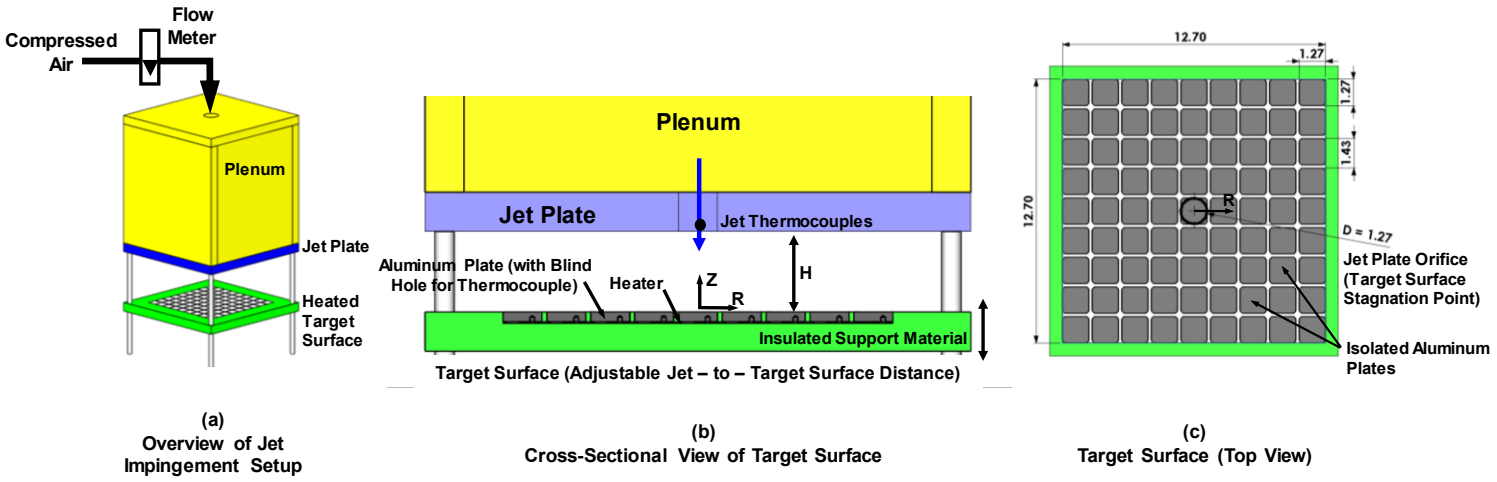

Figure 1: Overview of Jet Impingement Test Facility (units shown in cm)

$$\frac{Nu}{Re_{jet}^{0.76}} = \frac{24-\left|\frac{H}{D}-7.75\right|}{533+44\left(\frac{R}{D}\right)^{1.394}} \quad (1)$$

The application of impinging jets for heat transfer enhancement is not a novel approach. Both single jets and jet arrays have been investigated for decades. However, the studies used to quantify the heat transfer enhancement have been based on the measurement of surface and jet temperatures. While traditional, convective heat transfer experiments provide valuable information regarding surface heat transfer trends, they do not provide a comprehensive picture of the fluid development near the surface. For years, researchers have relied on CFD predictions to provide insight into the flow development near the heat transfer surface. This investigation applies the newly developed planar laser induced fluorescence (PLIF) method to measure near wall temperature gradients. These thermal profiles can be used to determine surface heat transfer coefficients while quantifying the thermal development of an impingement jet. The investigation builds on the work of Seitz and Wright [17] to demonstrate the use of the two-color PLIF technique for new wall flows.

For the current investigation, the PLIF method will be compared to a traditional, steady state heat transfer method. Using both the traditional method and PLIF, surface heat transfer coefficients will be obtained and compared. In addition, thermal profiles will be obtained showing the near – wall thermal development of the impinging jet. These results are obtained over a range of jet Reynolds numbers (5,000 – 15,000) and jet – to – target surface spacings (4 – 10).

EXPERIMENTAL FACILITY

General Overview of Jet Impingement Facility

A steady-state flat plate jet impingement facility is used for this investigation. **Figure 1** illustrates a sketch of the jet impingement test section (used for both traditional heat transfer and PLIF testing). The jet impingement setup consists of three main components: the plenum, jet plate, and target surface. The plenum and the jet plate are made from polycarbonate. The plenum provides uniform coolant flow (room temperature) to the jet plate through which the coolant flow moves to impinge on the hot target surface. A single round hole with a diameter of 0.0127 m is placed in the middle of the jet plate (jet length – to – diameter [L/D] = 1). Two standard T-type thermocouples are placed in the plenum near the jet exit to record the coolant flow temperature. The target plate surface consists of 81 aluminum plates, each measuring 0.0127 m × 0.0127 m × 0.318 cm (thick). A narrow 1.6 mm strip of silicone-based adhesive insulates the plates from one another. A standard T-type thermocouple is imbedded within each aluminum plate using a high thermally conductive, two component adhesive.

Beneath the aluminum plates is a custom, flexible, silicone-rubber heater placed between the plates and the support base. The aluminum plates are covered with a thin layer of thermally conductive, silicone paste to minimize contact resistance between the heater and the plates. A variable transformer is used to regulate the voltage to the heater and achieve the desirable power for the heater. With a constant heat flux being applied to the target surface, the surface temperature distribution is monitored, so the maximum wall temperature does not exceed 345K. The measured surface temperatures are coupled with the measured jet temperature to provide a distribution of regionally averaged heat transfer coefficients.

Four threaded rods and hex nuts are used to connect the target surface to the plenum. Loosening the nuts and sliding the target surface up and down changes the jet – to – target surface spacing. For the current investigation, the effect of jet plate to target surface is considered by varying this distance from 4D – 10D.

Cooling air is supplied to the plenum from a compressed air source. The flowrate of the cooling air is monitored using an inline rotameter. The flow rate is varied to achieve the desired jet Reynolds number. For the current investigation, tests are performed for impinging jets with Reynolds numbers of 5,000, 10,000, and 15,000.

For traditional experiments to obtain only surface heat transfer coefficients, this experimental setup is sufficient. However, with the inclusion of thermal field distributions from the PLIF technique, more instrumentation is required to support the seeding and imaging of the flowfield.

PLIF Setup for Jet Impingement

The PLIF experiments utilize the same setup described above for the steady state heat transfer tests. In addition to the basic impingement setup, a seeding and imaging system is required for the PLIF diagnostics. A schematic figure of the PLIF setup is presented in **Figure 2**. This figure includes an inset for both the PLIF calibration and the jet impingement tests.

As described by Seitz and Wright [17] the current two-color PLIF method is based on the fluorescence properties of toluene. Therefore, the compressed air must be seeded with toluene

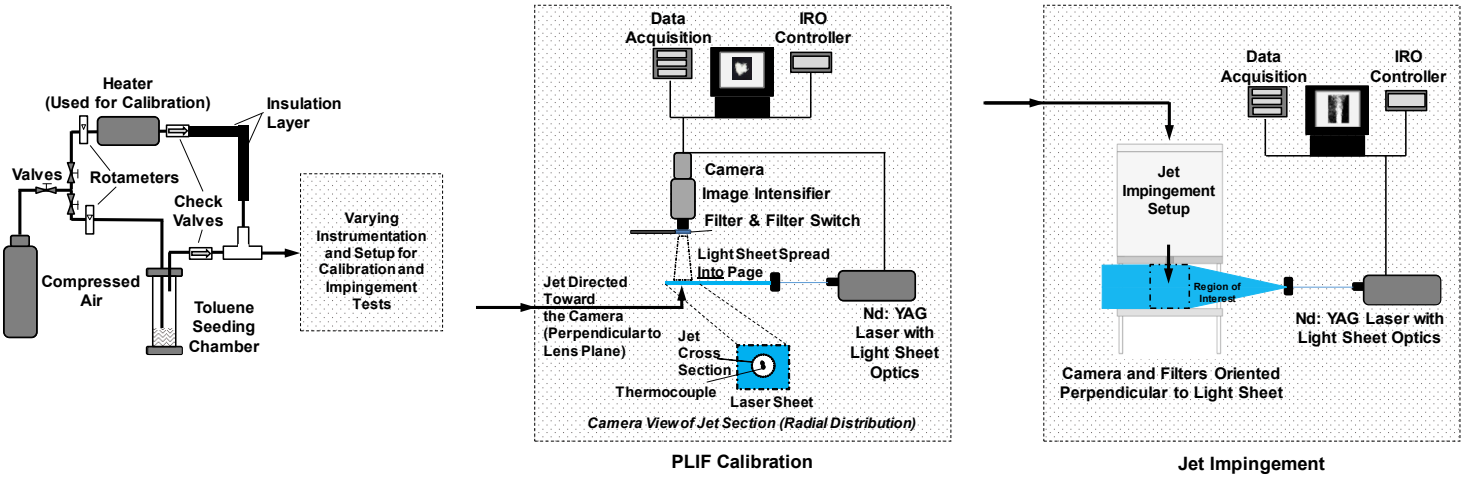

Figure 2: PLIF Setup for Calibration and Jet Impingement Tests

particles. To create and disperse the particles, a 0.0762 m diameter chamber is used to create a saturated mixture of toluene gas and air. This mixture leaves the chamber and eventually travels into the impingement plenum. During the PLIF calibration, the air-toluene mixture is added to a "hot" air stream to maintain the range of air temperatures required to relate the fluorescence intensity to gas temperature.

In order to capture the fluorescence intensity of the toluene seed particles, the particles must be excited to an increased energy state, and the energy emission (fluorescence) must be captured. The toluene is excited using a Nd:YAG laser with optics to create a planar, light sheet in the area of interest. The laser produces 266 nm light sheet, required for the fluorescence of the toluene, and the duration of each laser pulse is 100 ns. The laser is capable of producing energy up to 120 mJ / cm^2.

The fluorescence of the toluene seed particles is captured with a scientific grade CCD camera (maximum frame rate of 30 frames per second) equipped with an image intensifier. The camera is synced with the laser using a separate controller. Two filters are required to capture the two different emission spectra of the toluene, so an automated filter switch is used to easily switch between the two required filters. The temperature dependent response (285 nm) and the temperature independent response (320 nm) are captured separately. For each response, 500 images are recorded, and the time averaged response is presented. As described below, the ratio of these two signals can yield the temperature distribution of the air-toluene mixture (independent of the toluene concentration).

DATA REDUCTION

Steady State Heat Transfer Experiment

The first set of data comes from a traditional, steady state heat transfer experiment. Regionally averaged heat transfer coefficients are measured on the heated target surface. The heated surface is cooled using a single jet impinging in the center of the aluminum plate matrix. Each aluminum plate has a thermocouple embedded in the plate, providing the surface temperature for each plate. With the high conductivity of the aluminum and the measured heat transfer coefficients, the calculated Biot number for each plate is significantly less than 0.1 indicating the single thermocouple measurement represents a constant temperature through the volume of each aluminum plate.

With this traditional method, the regionally averaged heat transfer coefficient can be calculated using Equation 2. The net heat transfer from each copper plate is the difference between the power supplied to the heater and miscellaneous heat losses. While the support structure is fabricated from a low conductivity material and insulated to minimize stray heat loss, it is not a perfect insulator, so conduction occurs through the support material. While the target plate is heated to a relatively low temperature, radiation from the surface is present. Therefore, a separate heat loss calibration is required to account for the various forms of heat loss. The heat loss magnitude is estimated for different surface temperatures (with no convection on the surface), and from this information, the heat loss for each plate at any temperature can be approximated. For the current set of tests and temperatures, the heat loss averages approximately 9.5% of the total power supplied to the heater. This net heat flux is combined with the measured jet and surface temperatures (measured using thermocouples) to yield the surface heat transfer coefficient.

$$h=\frac{\dot{q}''}{A\left(T_{wall}-T_{jet}\right)} \tag{2}$$

The heat transfer coefficient is presented non-dimensionally in the form of the Nusselt number. Using the jet diameter as the characteristic length, Equation 3 presents the regionally averaged Nusselt number.

$$Nu=\frac{hD}{k_f} \tag{3}$$

The uncertainty is calculated for all cases using the method proposed by Kline and McClintock [18]. The maximum uncertainty among all tests was observed for the case with H / D = 6 at the stagnation point, and is equal to 2.86 (8.67%). The measurement and calculation of the convective heat flux has the most significant contribution to the experimental uncertainty. The overall uncertainty is directly proportional to the approximation of the heat losses from the target surface.

The Nusselt number is calculated on the target surface using Eqns. 2 and 3. A single radial distribution of these Nusselt numbers are compared with those predicted by the correlation from Goldstein et al. [7] (Eqn. 1). Results over the range of Reynolds numbers and jet – to – target surface spacings are presented in **Figure 3**. The magnitude and radial trends of the Nusselt numbers measured in this investigation follow those predicted by the correlation. The slight elevation of the current Nusselt numbers near the edge of the target surface (R / D > 4) are likely observed due to the transition from the aluminum plates to the surrounding

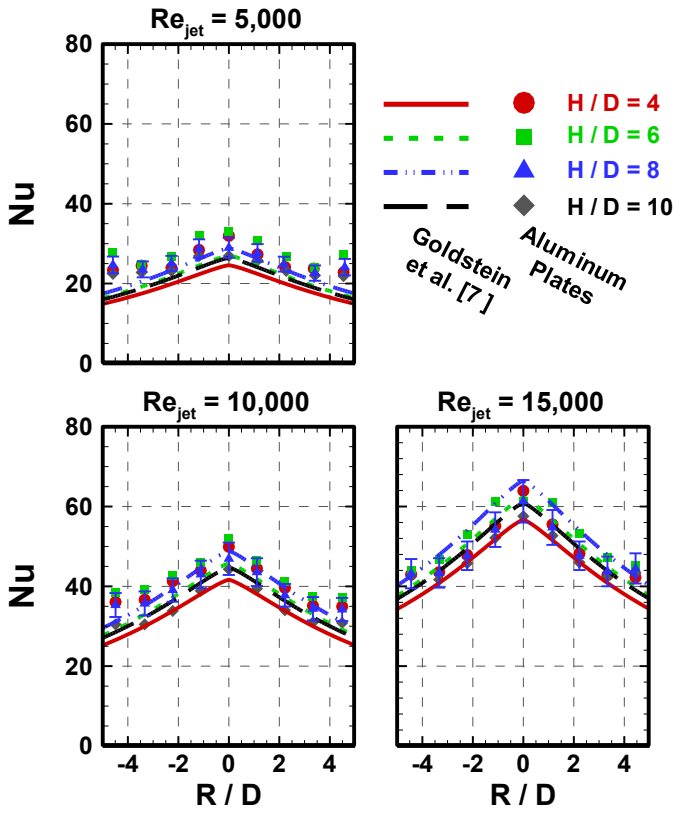

Figure 3: Regionally Averaged Nusselt Number Distributions (from Thermocouples)

support material. A notable difference occurs with the optimal jet – to – target surface spacing. Goldstein et al. [7] estimated that the maximum Nusselt number occurs at H / D = 8; however, for this study, the maximum Nusselt number is observed at H / D = 6. Goldstein et al. [7] developed the correlations for turbulent jets at relatively high Reynolds numbers (60,000 – 124,000) in comparison to this study (5,000 – 15,000). It was offered by Ashforth-Frost and Jambunathan [3] that there is a relation between the potential core length, jet – to – target surface spacing, and the maximum Nusselt number measured on the target surface. The Reynolds number affects the length of the potential core and that may explain the reason behind observing the maximum Nusselt number at a different H / D in comparison with Goldstein et al. It was reported by Ashforth-Frost and Jambunathan that the maximum Nusselt number occurs at 110% of the potential core length from the jet exit. The Goldstein et al. correlation provides an estimate for the Nusselt number; however, there are other factors such as potential core length that impact the Nusselt number.

PLIF Calibration and Method

Seitz and Wright [17] provide details of the PLIF calibration and basic methodology. The calibration is highlighted here along with the process to capture and analyze images. Elements regarding the spectral characteristics of the toluene can be found in prior work [17, 19].

In the basic PLIF experiment, the fluorescence of the tracer particle is recorded. This fluorescence emission is dependent upon a number of parameters including temperature, pressure, and seed concentration. By measuring the emission over two different wavelengths and taking a ratio of the two values, an intensity ratio is generated, and this ratio is a function of only the seed temperature. With these seed particles being excited within a plane created by the laser optics, the end result is a planar temperature distribution of the flow. However, in order to relate the measured intensity ratio to fluid temperature, a rigorous calibration must be completed.

As described by Seitz and Wright [17], a radial section of a free jet is used to produce the required calibration. As shown in Fig. 2, a heated jet of air (seeded with the toluene mist) is directed toward the camera, and intensity distributions are recorded within the jet cross section. Thermocouples are located within the cross-section to provide the relationship between the measured intensity and temperature. The temperature is varied from approximately room temperature to 400 K to cover the range of temperatures expected in the impingement study.

For each temperature of the calibration, as series of image sets are collected. Each image set consists of 500 images, and these images are averaged to provide a single, time averaged intensity distribution for each temperature and optical condition. For both the calibration and the impingement test, the following image sets are required:

(i) Reference (Blue Filter) – Laser on; flow seeded with toluene; room temperature
(ii) Reference (Red Filter) – Laser on; flow seeded with toluene; room temperature
(iii) Background @ Reference Temperature (Blue Filter) – Laser on; no toluene within the flow; room temperature
(iv) Background @ Reference Temperature (Red Filter) – Laser on; no toluene within the flow; room temperature
(v) Specific Temperature (Blue Filter) – Laser on; flow seeded with toluene; elevated temperature
(vi) Specific Temperature (Red Filter) – Laser on; flow seeded with toluene; elevated temperature
(vii) Background @ Specific Temperature (Blue Filter) – Laser on; no toluene within the flow; elevated temperature
(viii) Background @ Specific Temperature (Red Filter) – Laser on; no toluene within the flow; elevate temperature

The process to analyze these eight image sets includes background subtraction, time averaging, two-color thermometry, and normalizing of the fluorescence intensity. The offset from camera noise and surrounding light is removed by subtracting the background intensity. For this purpose, 500 background images are averaged and then the averaged background image is subtracted from each single PLIF image. At this time, the surrounding noise is eliminated from the PLIF images and they are ready to be time averaged. The two-color method is applied on the time averaged results; red filter intensities divided by blue filter intensities. The ratio eliminates the effect of seed concentration. Finally, the two-colored intensities are normalized by the two colored results at the reference temperature. The primary reason for normalizing is to reduce effects of inconsistencies in spatial illumination and camera sensitivity. Equation 4 shows the normalized intensity ratio.

$$I_N = \left(\frac{I_{Red} - I_{Back\text{-}Red}}{I_{Blue} - I_{Back\text{-}Blue}} \right)\Bigg|_T \Bigg/ \left(\frac{I_{Red} - I_{Back\text{-}Red}}{I_{Blue} - I_{Back\text{-}Blue}} \right)\Bigg|_{T_{Ref}} \quad (4)$$

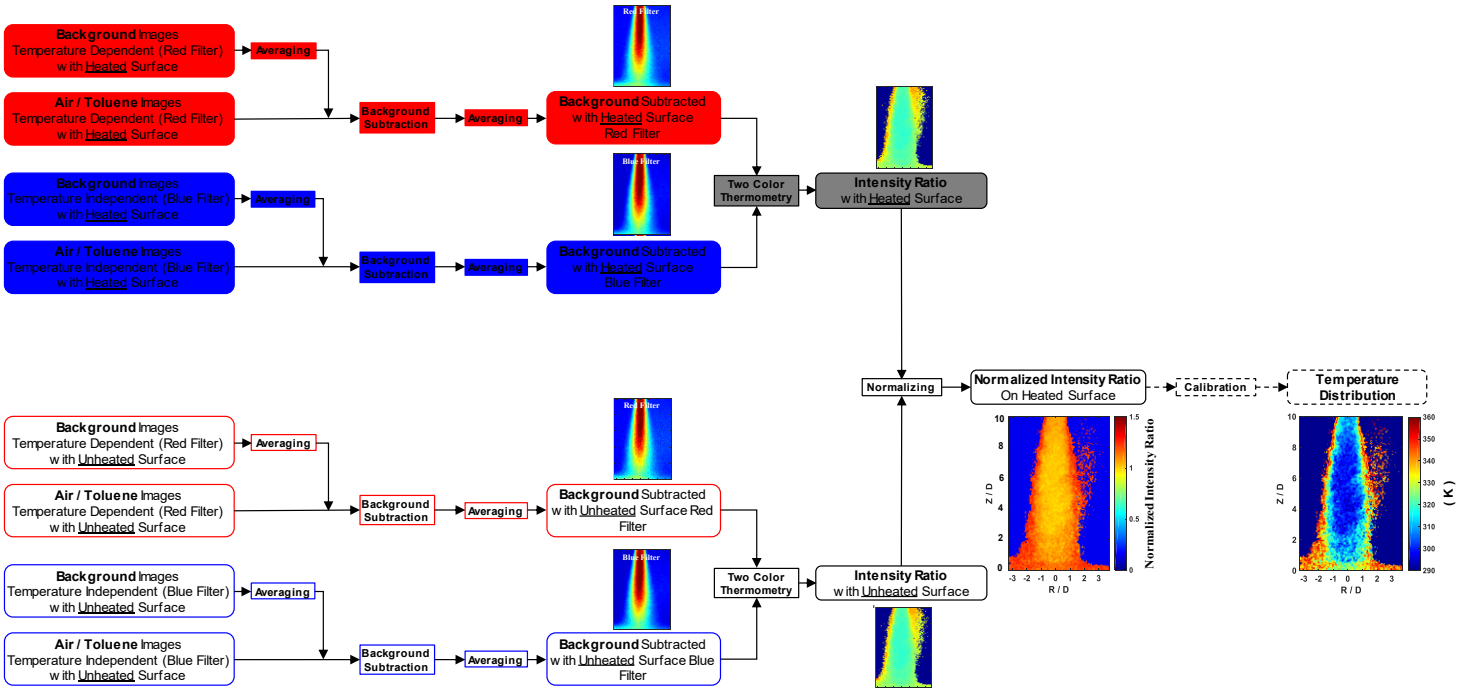

Figure 4: PLIF Data Reduction Procedure
(Including Sample Time Averaged Intensity, Intensity Ratio, and Temperature Distributions)

Figure 4 shows the basic flow chart for data collection and processing of the raw images. This flow chart is relevant to both the calibration and impingement procedures. The top set of images correspond to the "heated" temperatures, and the bottom set of images correspond to the images taken at the "reference" temperature. A sample calibration curve relating the normalized intensity ratio to the measured temperature ratio is shown in **Figure 5**. As described by Seitz and Wright [17] the curve represents data over a wide range of flow rates, seeding concentrations, and image quantities used in the data reduction process. As shown in the figure, the calibration data is captured within ±6% of the calibration equation.

For the impingement tests, the jet is at room temperature, and the target surface is heated. The data collection for this study consists of recording the same image sets as with the calibration. The reference images are taken while the mixture of air and toluene flows into the system at room temperature (297 K), the laser is on, and the target surface is not heated. After the target surface reaches the steady state condition (constant temperature at each aluminum plate), the toluene is introduced to the flow line from the seeding system. It is important to monitor the total flowrate to maintain the same Reynolds number. The air / toluene images are recorded while the laser in on.

The maximum area available with the current imaging system is equal to ten – by – six jet diameters. Having the jet at the center of the frame provides a maximum length of three jet diameters of the wall jet region (shown in Fig. 4). In order to capture a larger length, the camera is repositioned to view an area further from the center of the jet, and each test is repeated.

The post processing of the images includes the following steps: background subtraction, time averaging, two color thermometry, and normalizing the fluorescence intensity (I / I_{ref}). Included with the flow chart in Fig. 4 are sample distributions for the impinging jet (Re_{jet} = 10,000, H / D = 10).

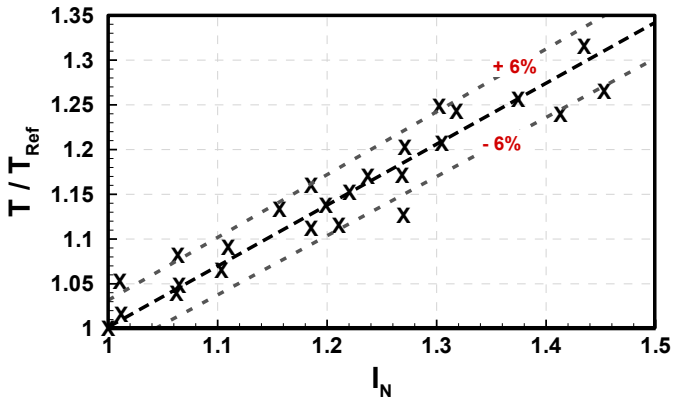

Figure 5: PLIF Calibration

Following the process of Seitz and Wright [17], the error of the planar temperature distributions is considered in terms of the standard deviation of the measurements. With the post processing of 500 images (for each image set), the maximum standard deviation is estimated to be ±12.5K (with measured fluid temperatures in the range of 300K – 350K. With the intensities of the temperature dependent and temperature independent emissions being relatively close in magnitude, the two-color thermometry step (intensity ratio) introduces the most error in the data reduction process. In the previous work [17], the final temperature distributions were also discussed in relation to the eight separate sets of images that are used to generate the detailed temperature distributions.

RESULTS AND DISCUSSION

Seitz and Wright [17] used the PLIF method to characterize the thermal development of a heated, free jet. This investigation expands the use of the PLIF technique to not only obtain thermal

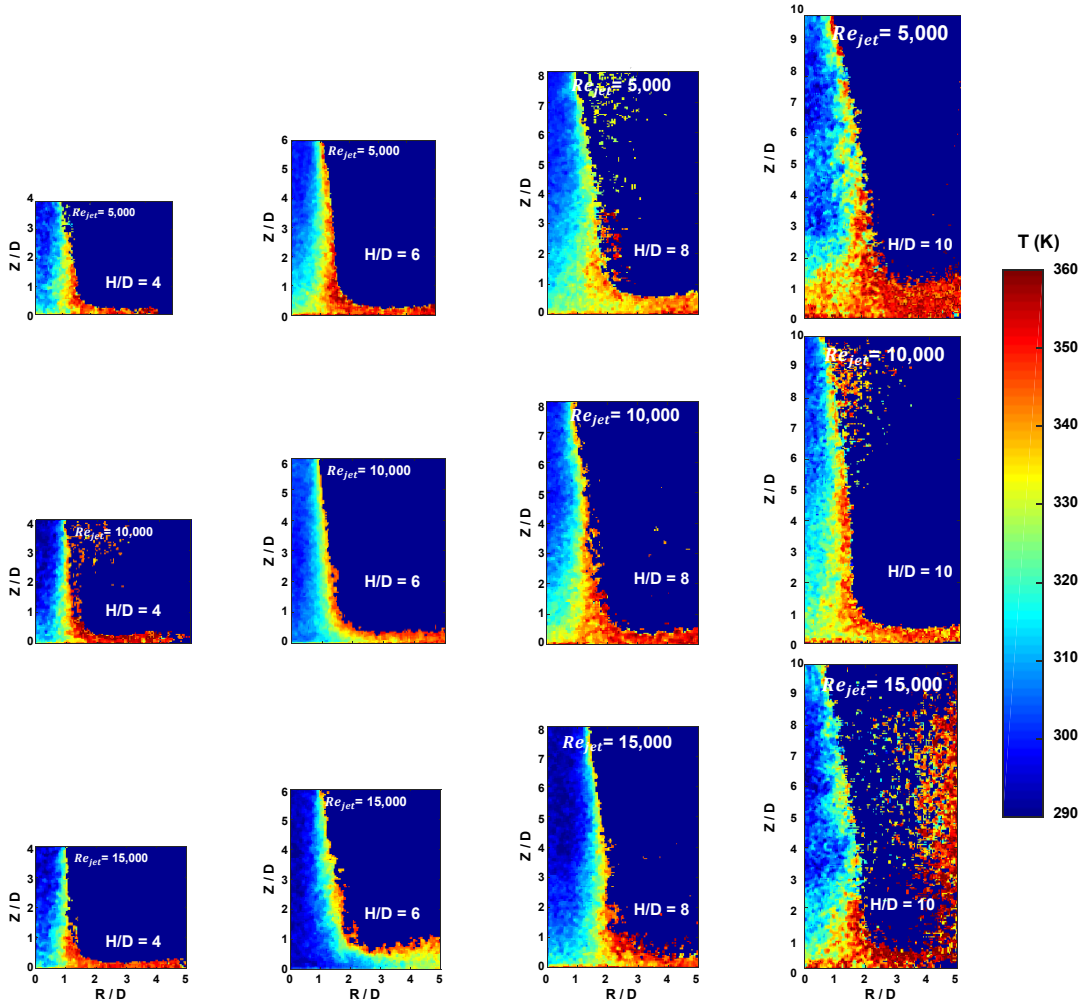

Figure 6: Detailed Temperature Distributions of Impinging Jets at Various Reynolds Numbers and Jet – to – Target Surface Distances

profiles, but also use the near wall temperature gradients to estimate the heat transfer coefficients on the surface. The impinging jet cools the heated surface, and based on the near wall temperature measurements of the impinging jet, surface heat transfer coefficients can be measured. These values are compared to those obtained through a more traditional heat transfer experiment.

Effect of Jet Reynolds Number

Detailed temperature distributions for impinging jet tests are shown in **Figure 6**. Temperature distributions are shown for "half" of the jet impinging on the heated surface. As mentioned previously, images were recorded with the camera centered on the center of the jet and placed off-center. These off-center images allow for more of the wall jet region to be visualized. A full presentation of the temperature distributions is provided by Seitz [20].

In Fig. 6, the three flow regions: free jet, stagnation, and wall jet, are distinguishable. The turbulent flow structures, shear layer formation, are more visible at the edge of the jets. Thus, higher mixing is expected to be observed at the edge. The PLIF results illustrate the impact of this mixing at the edge of the jets. The results for all cases show that the potential core region is unaffected by the radial growth of the shear layer. As the jet moves toward the target surface, in the downstream locations, the shear layer grows because of the instability of eddies.

A very thin boundary layer is formed in the stagnation zone. For the Reynolds numbers used in this study, the stagnation boundary layer remains laminar. However, turbulence in the impinging jet disturbs this thin boundary layer. Thus, the heat transfer is increased significantly. As the Reynolds number increases, the turbulence in the impinging jet also increases, and therefore, more disruption occurs within the boundary layer. As can be seen in the figure, the temperature gradient increases near the stagnation region with an increase in jet Reynolds number. This effect of heat transfer transition is also observed at the wall jet region. As an example, it is seen there is no significant temperature gradient within the wall jet region for Re_{jet} = 5,000. As the Reynolds number increases, a higher temperature gradient is observed within the region. This happens because at a lower Reynolds number, the mixing impact is lower, and the jet loses its effectiveness as it covers the target surface in the wall jet region. As the jet Reynolds number increases, the instability within that region increases. Therefore, the jet retains its cooling effectiveness through this region.

For cases with greater jet – to – target surface spacing, for a lower Reynolds number, a thicker boundary layer is observed. As the Reynolds number increases, the boundary layer gets thinner. Flow separation is observed for cases with H / D = 10 as fluid

travels towards the wall jet region (in the radial direction). As an example, for impinging jet with Re_{jet} = 15,000 and H / D = 10, flow slips on the surface at R / D approximately equal to three. The impact of this separation increases as the Reynolds number increases. This may be related to the reduction of the kinetic energy transportation within the boundary layer in the wall jet region. As kinetic energy transportation reduces, the potential energy increases, and therefore, the fluid pressure increases. The increase in pressure may slow the fluid on the surface or even cause reversed flow. More study on flow momentum is required to achieve a better understanding of the flow separation that is observed.

Another interesting phenomena is observed for Re_{jet} = 15,000, H / D = 10. With the relatively large flow rate and jet – to – target surface spacing, it becomes apparent the volume of air within the impingement cavity is heating. While the field of view does not extend beyond R / D = 5, it appears as the wall jet separates from the surface, the coolant is creating a region of recirculation within the impingement cavity. This is not observed at smaller H / D as the wall jet is accelerating from the impingement cavity.

To have a consistent comparison between data, a dimensionless temperature, η, is defined as Equation 5. The dimensionless temperature is used to compare the effect of jet Reynolds number and jet – to – target plate spacing among the PLIF experimental cases. The wall and ambient temperatures come from thermocouple data, and the local jet temperature, T, is extracted from the PLIF data. The dimensionless temperature varies in the range of zero to one. For η equal to zero, the jet impingement temperature is equal to the ambient temperature, as the value of η increases, the jet temperature gets closer to the surface temperature; η = 1 means that the jet temperature is equal to the wall temperature at a specific radial location.

$$\eta = \frac{T - T_{\infty}}{T_{wall} - T_{\infty}} \tag{5}$$

The dimensionless temperature presents the effectiveness of the impinging jet for cooling the plate. The dimensionless temperatures are calculated for all cases using Eqn. 5. The effectiveness distribution at the stagnation point (R / D = 0) for all cases are presented in **Figure 7**. For Re_{jet} = 5,000, the jet effectiveness is similar for cases with H / D = 4, 6, and 8. As the Reynolds number increases, the dependency of the jet effectiveness on the jet – to – target spacing increases. For all cases, the maximum jet effectiveness at the stagnation point is observed for cases with a jet – to – target surface spacing of 6 and the minimum is observed for cases with a jet – to – target surface spacing of 10.

To study the Reynolds number dependency, the results of the dimensionless temperature are also categorized for the three Reynolds numbers at each jet – to – target surface spacings in Fig. 7. Comparing the results indicates that the effectiveness at the stagnation point is relatively independent of the Reynolds number, however; a dependency on jet – to – target surface spacing is observed.

Thermal boundary layer dependency on the jet Reynolds number and jet – to – target surface spacing is seen through PLIF results. The thermal boundary layer is defined as the distance from a target surface where the temperature is equal to 99% of the ambient temperature. According to Equation 5, the thermal boundary layer can be measured where η approaches zero. **Figure 8** presents the dimensionless temperature for cases with a jet – to – target surface spacing of 4 and 8 (Re_{jet} = 5,000), at different radial

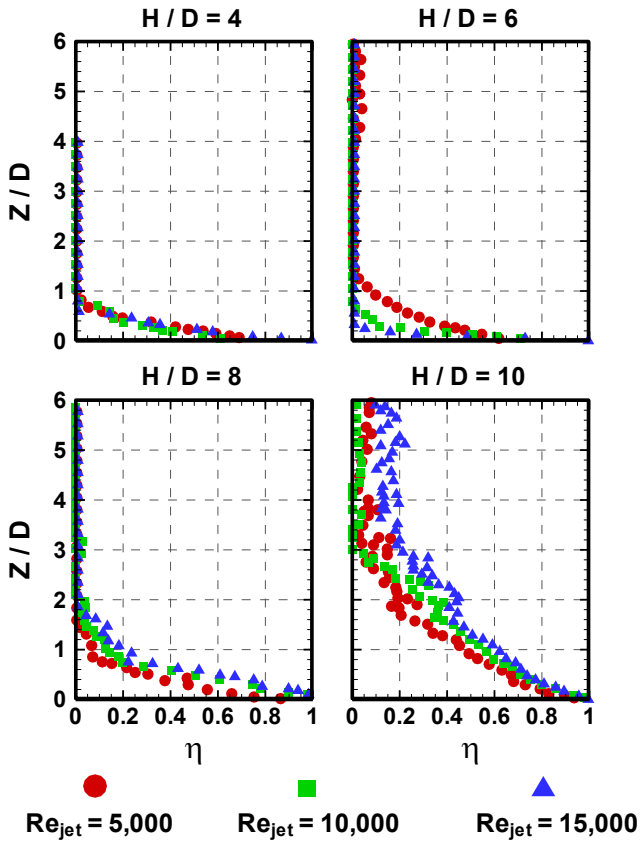

Figure 7: Non-dimensional Temperature Profiles at R / D = 0 (Stagnation Point)

locations. It can be seen that the thickness of the boundary layer increases as the jet travels away from the stagnation point. It is expected to observe a decrease in the heat transfer rate, and as a result, a decrease in the temperature gradient. Figure 8 demonstrates the temperature gradient decreases as the distance from the stagnation point increases.

Thermal Boundary Layer Measurement Using PLIF

The single jet impingement setup is used to validate the novel PLIF technique. A sample of thermal profiles obtained using the PLIF technique have been presented. A full presentation of the acquired temperature profiles are available from Seitz [20]. Using the local temperature profile, local Nusselt numbers can be calculated. For the current work these Nusselt numbers obtained from the PLIF technique are compared with the results from the traditional, steady state heat transfer test. First, the local heat transfer coefficients are obtained from combining Fourier's and Newton's laws as expressed in Equation 6.

$$h = \frac{-k_f \left.\frac{\partial T}{\partial Z}\right|_{Z=0}}{T_{wall} - T_{jet}} \tag{6}$$

Thermocouples provide the surface temperatures, and the jet outlet temperature is directly extracted from the PLIF results. In order to calculate the wall temperature gradient of Eqn. 6, relations between temperature and vertical distance from the surface (Z) are built at the stagnation point (R / D = 0), R / D = 1.125, and R / D = 2.250. The temperature profile is extracted from PLIF results and Z is the location above the surface. In order to estimate the

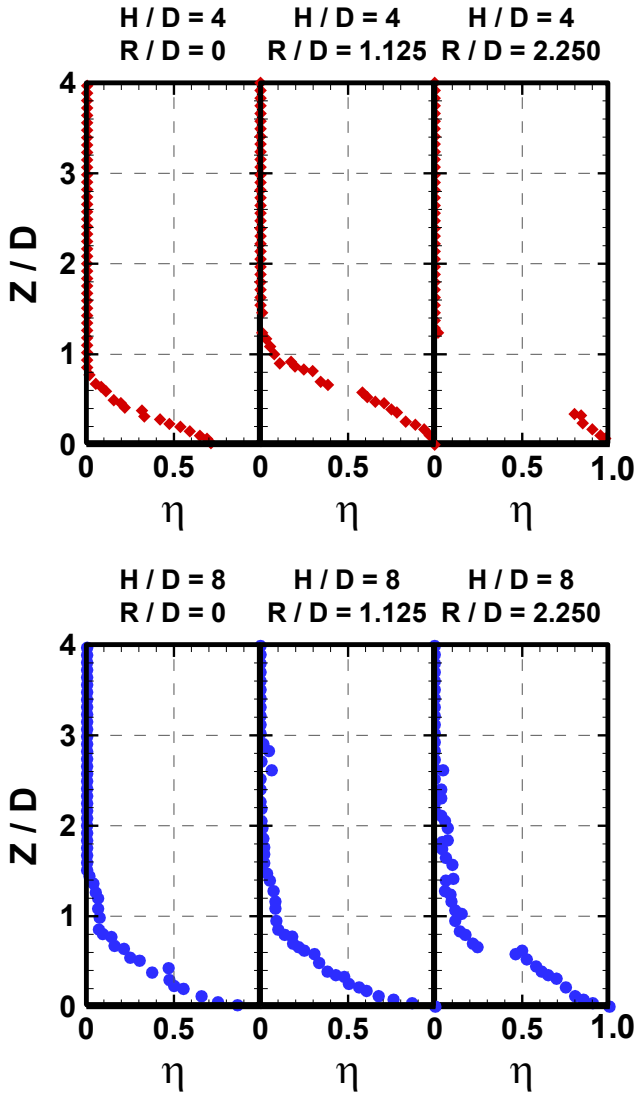

Figure 8: Non-dimensional Temperature Profiles at Various Radial Locations (Re_{jet} = 5,000)

derivative in the viscous sublayer, the first three pixels above the surface are selected to build the temperature equation as a function of location. Then, $\partial T/\partial Z$ can be obtained at the surface (Z = 0). After the heat transfer coefficient is obtained, the Nusselt number is calculated using Eqn. 3.

The same procedure was repeated for all cases and compared with the Nusselt numbers calculated using the steady state, traditional heat transfer experiment. The results of the comparison between the PLIF and thermocouple results are shown in **Figure 9**. The results show that the Nusselt number calculated from combining the Fourier and Newton's law are in a good agreement with the Nusselt number obtained from the traditional method. The maximum error offset ($(Nu_{PLIF} - Nu_{Traditional})/Nu_{Traditional}$) among all cases is equal to 8.75%.

As shown in Fig. 9, the PLIF method has provided Nusselt number distributions on the flat target surface. The trends have echoed those of traditional heat transfer tests including enhanced heat transfer with increasing Reynolds number and decreasing jet – to – target surface spacing (with an optimum value ranging from 5 to 7 jet diameters). The most significant variation between the PLIF and surface heat transfer data occurs with H / D = 4. The

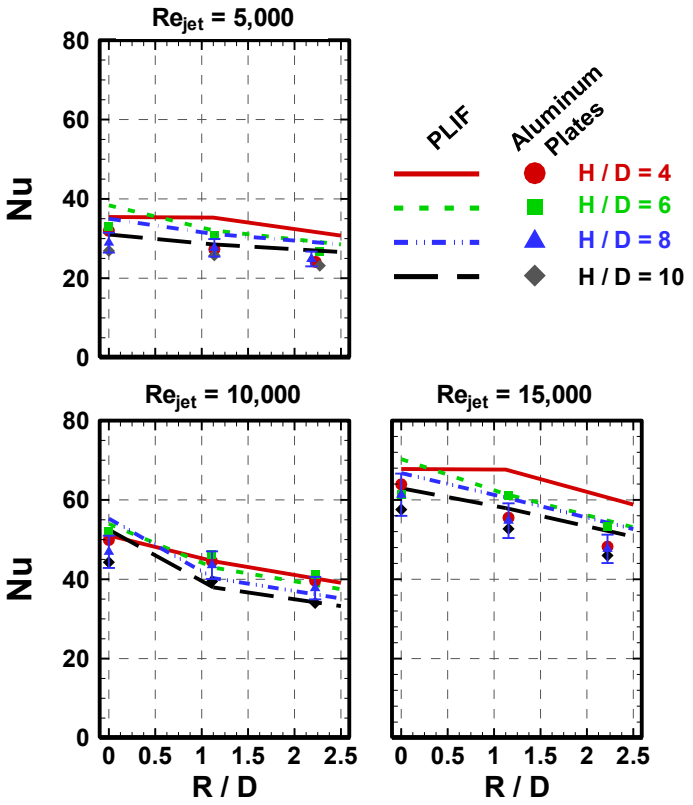

Figure 9: Measured Nusselt Numbers from PLIF and Traditional Heat Transfer Method

PLIF technique identifies the maximum heat transfer occurring at this small jet – to – target surface spacing. With the PLIF technique, the challenge is to measure temperature gradients within flow fields where the temperature difference is relatively small. At H / D = 4, the potential core strikes the target surface at the stagnation point, and the cooling jet is quickly heated along the surface. In addition, the PLIF measurements are recorded in a steady state system, so the quiescent air within the impingement cavity is expected to be warmer than the surrounding environment (and the jet). Therefore, as the cool jet strikes the surface, both the hot surface and the warm, stagnant air within the cavity heat it. The limited spatial resolution of the seeded flow makes it difficult to fully resolve the thermal profile. This problem is lessened as the jet – to – target surface spacing increases, as there is more space within the impingement cavity.

It is understood, similar, more refined heat transfer coefficient distributions could be obtained using a wide variety of surface measurement techniques. However, with the inclusion of heat transfer coefficient distributions, the versatility of the method is further demonstrated. The proposed two-color PLIF technique provides quantitative thermal diagnostics of the flow and can be used to obtain surface heat fluxes. Up to this point, obtaining this information would require at least two separate experiments (with independent hardware), and methods capable of fully resolving the thermal behavior of the flow are limited. In addition, the application of this technique to traditional, three-temperature problems (film cooling), will also provide experimental validation of the thermal characteristics associated with the near wall mixing phenomena. While improvements to the method are still forthcoming, the technique has shown the ability to experimentally consider heat transfer problems from a new perspective.

General Discussion of PLIF for Thermal Gradients

Time averaged, steady state temperature distributions have been obtained in this study through rigorous data acquisition and data processing procedures. The time averaging, two-color thermometry, and normalizing steps introduce scatter within the profiles; however, these steps are also necessary to reduce the bias error within the setup. Moreover, the need for large sets of images also provides an opportunity to study the turbulent, temperature characteristics of the flow. Using the individual images from each image set provides an opportunity to consider the instantaneous temperature fluctuations developing within the flow.

In addition, the technique can be expanded to more complex flow fields to understand how thermal gradients develop within mixed flows. For example, the PLIF technique can be applied to film cooling models, to investigate the gradients seen as the mainstream and coolant mix on the cooled surface. The technique can also be applied to a two-dimensional jet impingement array. With strong crossflow effects, it is often difficult to ascertain the driving fluid temperature for surface heat transfer. This PLIF method could provide two-dimensional temperature distributions within the impingement chamber to understand how the jet temperature varies from the jet plate to the target surface in the presence of confined crossflow. In addition to these examples, the PLIF method is also capable of providing quantitative data to support CFD simulations.

In recent years, the magnetic resonance imaging (MRI) has also been used to obtain temperature (concentration) distributions within complex flows. Stanford University has developed a method capable of simultaneously measuring velocity (MRV) and concentration (MRC) distributions [21 – 23]. Applying a mass transfer analogy to the concentration measurements, allows for the acquisition of a non-dimensional, mixed temperature. In addition, these distributions can be acquired "near" the cooled surface to provide approximate, surface film cooling effectiveness distributions. As the name implies, PLIF measurements are restricted to a single plane within the flow. To characterize multiple planes within a domain, the laser light sheet must traverse through the flow. In contrast, MRC measurements are gathered through the entire volume of fluid without the restriction of optical access. The obvious drawback for the MRC / MRV measurements is the availability of an MRI machine.

A wide range of scientific instrumentation is becoming more readily available. Coupling the instrumentation with improved computing resources has opened the door for the development of new experimental methods. Experientialists are able to acquire highly resolved data in both space and time. For decades, researchers have used cameras to obtain detailed "surface" distributions, and now the task of resolving the flowfields is at hand. For the current, single impinging jet setup, the cost of implementing the PLIF technique does not justify its use. However, the demonstration of the technique does show the potential of the method to be applied to more complex fields, especially in mixing problems. With the application of the technique to more flow scenarios, the robustness of the method will be tested, and the capabilities will be fully realized.

CONCLUSIONS

The application of the PLIF technique on a single impingement jet has been presented. The PLIF technique was applied to several impingement tests at different Reynolds numbers and jet – to – target surface spacings for validation of the proposed method. This method was validated against regionally averaged Nusselt numbers using traditional heat transfer calculations. Results show that the proposed PLIF method is capable of resolving a near wall thermal boundary layer. PLIF provides a detailed distribution of the temperature, and provides the opportunity to fully study the structure the thermal field without disturbing the flow. The PLIF method also has the potential to visualize the turbulent structure and flow thermal behavior simultaneously. This opens new opportunities to gain better understanding of complex physics and improve the available correlations that are being used in computational fluid mechanics tools.

ACKNOWLEDGEMENTS

This work has been sponsored by the National Science Foundation under award number CBET-1126371. The authors would like to thank Drs. Truell Hyde and William Jordan of Baylor University for their support of this project. In addition, the machine work (and advice) of Mr. Ashley Orr was vital to the completion of the work.

REFERENCES

[1] Han, J.C, Dutta, S. and Ekkad, S., 2012, *Gas Turbine Heat Transfer and Cooling Technology,* 2nd ed., CRC Press.

[2] Bergman, T.L., Lavine, A.S., Incropera, F.P., and Dewitt, D. P., 2011, *Fundamentals of Heat and Mass Transfer*, 7th ed., John Wiley & Sons.

[3] Ashforth-Frost, S. and Jambunathan, K., 1996, "Effect of Nozzle Geometry and Semi-Confinement on the Potential Core of a Turbulent Axisymmetric Free Jet," *International Communications in Heat and Mass Transfer*, 23(2), pp. 155–162.

[4] Martin, H., 1977, *Advances in Heat Transfer*, Elsevier, pp. 1–60.

[5] Jumbunathan, K., Lai, E., Moss, M., and Button, B.L., 1992, "A Review of Heat Transfer Data for Single Circular Jet Impingement," *International J. Heat and Fluid Flow*, 13(2), pp. 106–115.

[6] Polat, S., Huang, B., Mujumdar, A.S., and Douglas, W.J.M., 1989, "Numerical Flow and Heat Transfer Under Impinging Jets: A Review," *Annual Review of Heat Transfer*, 2(2), pp. 92–110.

[7] Goldstein, R.J., Behbahani, A.I., and Heppelmann, K.K., 1986, "Streamwise Distribution of the Recovery Factor and the Local Heat Transfer Coefficient to an Impinging Circular Air Jet," *International J. Heat and Mass Transfer*, 29(8), pp. 1227–1235.

[8] Lee, S.J., Lee, J.H., Lee, D., and Greif, R., 1993, "Heat Transfer from a Plate to a Fully Developed Axisymmetric Impinging Jet," ASME Winter Annual Meeting, New Orleans, LA.

[9] Donaldson, C.D., Snedeker, R.S., and Margolis, D.P., 1971. "A Study of Free Jet Impingement. Part 2. Free Jet Turbulent Structure and Impingement Heat Transfer," *J. Fluid Mechanics*, 45(3), pp. 477–512.

[10] Goldstein, R.J. and Behbahani, A.I., 1982, "Impingement of a Circular Jet with and without Cross Flow," *International J. Heat and Mass Transfer*, 25(9), pp. 1377–1382.

[11] Mohanty, A.K. and Tawfek, A.A., 1993, "Heat Transfer due to a Round Jet Impinging Normal to a Flat Surface," *International J. Heat and Mass Transfer*, 36(6), pp. 1639–1647.

[12] Baughn, J.W. and Shimizu, S., 1989, "Heat Transfer Measurements from a Surface with Uniform Heat Flux and an Impinging Jet," *ASME J. Heat Transfer*, 111(4), pp. 139–147.

[13] Huang, L. and El-Genk, M. S., 1994, "Heat Transfer of an Impinging Jet on a Flat Surface," *International J. Heat and Mass Transfer*, 37(13), pp. 1915–1923.
[14] Hoogendoorn, C., 1977, "The Effect of Turbulence on Heat Transfer at a Stagnation Point," *International J. Heat and Mass Transfer*, 20(12), pp. 1333–1338.
[15] Lytle, D. and Webb, B.W., 1994, "Air Jet Impingement Heat Transfer at Low Nozzle-Plate Spacings," *International J. Heat and Mass Transfer*, 37(12), pp. 1687–1697.
[16] Goldstein, R.J. and Timmers, J.F., 1982, "Visualization of Heat Transfer from Arrays of Impinging Jets," *International J. Heat and Mass Transfer*, 25(12), pp. 1857–1868.
[17] Seitz, S. and Wright, L.M., 2019, "Thermal Characterization of a Turbulent Free Jet with Planar Laser Induced Fluorescence (PLIF)," ASME Paper No. GT2019-92058.
[18] Kline, S.J., and McClintock, F.A., 1953, "Describing Uncertainties in Single-Sample Experiments," Mech. Eng. (Am. Soc. Mech. Eng.), 75, pp. 3-8.
[19] Koban, W., Koch, J.D., Hanson, R.K., and Schulz, C., 2004. "Absorption and Fluorescence of Toluene Vapor at Elevated Temperatures," *Physical Chemistry Chemical Physics*, 6(11), pp. 2940–2945.
[20] Seitz, S., 2018, *Thermal Boundary Layer Measurements using Planar Laser Induced Fluorescence*, Ph.D. Dissertation, Baylor University.
[21] Benson, M.J., Elkins, C.J., and Eaton, J.K., 2011, "Measurement of 3D Velocity and Scalar Field for a Film-Cooled Airfoil Trailing Edge," *Experiments in Fluids*, 51(2), pp. 443 – 455.
[22] Spirnak, J., Samland, M., Tremont, B., McQuirter, A., Williams, E., Benson, M., Van Poppel, B., VerHulst, C., Elkins, C., Burton, L., Eaton, J., and Owkes, M., 2016, "Validation of Magnetic Resonance Thermometry through Experimental and Computational Approaches," 52nd AIAA / SAE / ASEE Joint Propulsion Conference.
[23] Issakhanian, E., Elkins, C.J., and Eaton, J.K., 2016, "Film Cooling Effectiveness Improvements Using a Nondiffusing Oval Hole," *ASME J. Turbomachinery*, 138(4), Article 041004, 6 pages.